International Journal of Applied Mechanics
Vol. 12, No. 8 (2020) 2050095 (29 pages)

DOI: 10.1142/S1758825120500957

Electromechanical Coupling and Energy Conversion in a PZT-Coated Acoustic Black Hole Beam

Linli Zhang

Department of Mechanical Engineering
The Hong Kong Polytechnic University
Hung Hom, Kowloon, Hong Kong SAR, P. R. China
linli-me.zhang@connect.polyu.hk

Gaetan Kerschen

Department of Aerospace and Mechanical Engineering
University of Liège, Allée de la Découverte 9
B-4000 Liège, Belgium
g.kerschen@uliege.be

Li Cheng*

Department of Mechanical Engineering
The Hong Kong Polytechnic University, Hung Hom
Kowloon, Hong Kong SAR, P. R. China
li.cheng@polyu.edu.hk

Received 24 June 2020
Revised 17 August 2020
Accepted 29 August 2020
Published 7 November 2020

The phenomenon of acoustic black hole (ABH) exhibits unique and appealing features when bending waves propagate along a structure with a tailored power-law thickness profile. The ABH-induced wave retarding and energy focussing are conducive to effective wave manipulation and energy harvesting. Using a PZT-coated ABH beam as a benchmark, this paper investigates the electromechanical coupling between the PZT patches and the host beam and explores the resultant energy conversion efficiency for potential energy-harvesting (EH) applications. An improved semi-analytical model, considering the full coupling among various electromechanical components in the system, is proposed based on Timoshenko deformation assumption and validated through comparisons with FEM and experimental results. Numerical analyses are then conducted to show typical ABH-specific features as well as the influence of the PZT layout on the electromechanical coupling of the system and the corresponding EH efficiency. Results show that ABH effects entail effective and broadband EH upon proper design of the system with due consideration of the PZT layout in relation to the wavelength and frequency range. Some design guidelines on the installation of PZTs are provided in view of maximization of the ABH benefits and the energy-harvesting performance.

Keywords: Acoustic black hole; electromechanical coupling; vibration energy harvesting; broadband energy focussing.

*Corresponding author.

1. Introduction

Due to its vital role in a wide range of engineering applications, manipulation of structural wave propagation has been arousing persistent interests in the scientific community. Among numerous efforts, the exploration of the so-called acoustic black hole (ABH) effect has attracted widespread attention and experienced a major growth in the past few years as reviewed in recent papers [Chong *et al.*, 2017; Pelat *et al.*, 2020]. The ABH effect rests on the propagation properties of structure-borne flexural waves in thin-walled structures. By tailoring the thickness profile of the structure according to a reducing power-law relationship, the local phase (and the group) velocity of the propagating flexural waves gradually reduces while approaching the thinnest part [Mironov, 1988; Krylov, 1998], as shown in Fig. 1. In the ideal scenario in which the thickness becomes zero, wave reflection is annulled, thus causing high energy concentration which can be effectively dissipated using a small amount of damping materials [Krylov, 2004; O'Boy and Krylov, 2011]. The phenomenon is shown to persist above the so-called cut-on frequency [Conlon *et al.*, 2015] when the wavelength becomes comparable with the size of the ABH. As a result, ABH effect exhibits broadband features, which are conducive to conceiving lightweight and highly damped structures/structural components. The unique ABH properties offer new possibilities and may trigger innovative engineering applications. Apart from a series of fundamental works on ABH-specific phenomena and their quantifications [Denis *et al.*, 2014; Ouisse *et al.*, 2019; Aklouche *et al.*, 2016; Leng *et al.*, 2020; Hook *et al.*, 2019], the ABH effect has also been explored for major applications such as vibration control, structural sound radiation and energy harvesting (EH) [Pelat *et al.*, 2020].

ABHs for vibration control mainly rely on the high energy dissipation inside the ABH area of a structure as a result of the broadband energy trapping and focussing. Existing researches allow for a good understanding of the physical process, as well as various means to enhance the ABH effects for effective vibration mitigation [Krylov, 2004; O'Boy and Krylov, 2011; Tang and Cheng, 2017a; Zhao and Prasad,

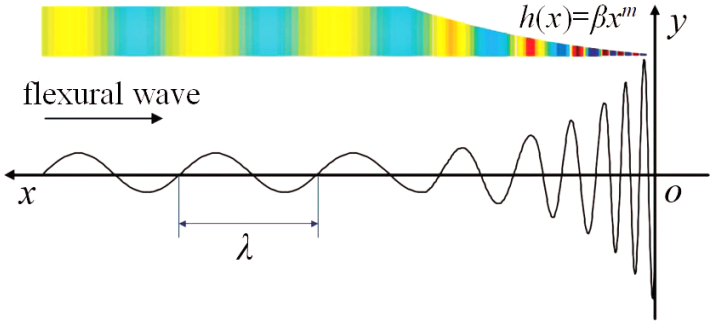

Fig. 1. Schematic diagram showing flexural wave propagation in 1D ABH structure.

2019]. ABH features can either be embedded into a structure [Conlon and Feurtado, 2018; Kralovic and Krylov, 2007] or added to an existing structure as an add-on device [Zhou and Cheng, 2018], designed in more or less sophisticated forms [Zhou *et al.*, 2017; Lee and Jeon, 2017]. They can also be used in a periodic lattice, which warrants exceptional band gaps within which wave propagations are prohibited. Illustrations have been made using 1D [Tang and Cheng, 2017b,c] and 2D [Tang and Cheng, 2019] structures, in which an effective merging of the ABH-induced local resonances and Bragg scattering entails effective energy insulation using a small number of ABH cells.

The second application capitalizes on the ABH-specific wave-retarding phenomena to control sound radiation in either a free [Feurtado and Conlon, 2017; Ma and Cheng, 2019a; Bowyer and Krylov, 2015; Li and Ding, 2019] or closed space [Ji *et al.*, 2019]. The ABH-induced reduction in the wave speed in solid allows for the conversion of the structural supersonic waves into subsonic ones (compared with the sound speed in air) so that their sound radiation efficiencies are greatly impaired, thus entailing a significant reduction in its sound radiation in free field [Feurtado and Conlon, 2017; Ma and Cheng, 2019a]. When used as a cavity wall, an ABH panel reduces the spatial coupling with the acoustic cavity, thus also resulting in reduced sound radiation into the cavity [Ji *et al.*, 2019b].

The strong energy concentration inside the ABH area also offers an ideal scenario for high efficiency EH. Surprisingly, as compared with the aforementioned two applications, ABH-based EH has not received sufficient attention up to now. Compared with other existing EH methods based on various physical mechanisms [Safaei *et al.*, 2019; Solovyev and Duong, 2016], particularly the vibration-based EH using uniform beams, ABH shows its promising potentials, which were first investigated by Zhao *et al.* [2014, 2015a,b]. Using five ABH cells on a beam, covered with uniform piezoelectric patches, the coupled electro-mechanical system was investigated through finite element method (FEM) simulations. Results show that an ABH beam outperforms a uniform beam in terms of harvested electrical power. Maugan *et al.* [2019] proposed an equivalent ABH structure formed by piezoelectric sensors to create a gradual variation of the equivalent Young's modulus along the beam. The concentrated mechanical energy at the beam center was harvested by piezoelectric device in both weak and strong coupling cases. More recently, Zhao and Prasad [2018] investigated vibration EH using a cantilever beam with a modified ABH cavity. Ji *et al.* [2019a] analyzed and experimentally tested a double-layer compound ABH beam, over which multiple piezoelectric patches were used for EH. The use of an array comprising PZTs cut into small slices was to avoid possible neutralization of the opposite electrical charges which would have been produced by a single PZT layer. The system was however intuitively designed, though the basic principles were validated through FEM analyses. Generally speaking, despite case-by-case demonstrations on some individual EH designs, there seems to be a lack of general investigation on the fundamental aspects of the ABH-based EH as

well as the provision of clear criteria to guide the system design to maximize the EH efficiency.

Indeed, the design of an effective EH system relies on the effective electromechanical coupling between the host mechanical structure and the EH devices such as PZTs. In the context of ABH-based EH, this coupling becomes more delicate due to the weakened structural stiffness of the ABH structure, especially within the ABH area, which requires a meticulous handling. Meanwhile, numerous parameters involved in the physical process, relating to both the host structure and the EH devices, make the design of an effective ABH-based EH system extremely challenging. This obviously requires an efficient and flexible simulation tool, which is capable of coping with the aforementioned challenges.

The unique wave propagation pattern inside an ABH structure results in a highly non-uniform wavelength distribution inside the structure, thus posing challenges to the system modeling. On the top of that is the need of reaching high frequency range, which is also a difficult task by itself even for a uniform structure [Zhang and Cheng, 2017]. Typical simulation methods used in ABH research mainly include geometric acoustic approximation method [Krylov, 1989], impedance matrix method [Li and Ding, 2019], Rayleigh–Ritz method [Tang *et al.*, 2016] and predominantly the finite element (FE) method [Conlon *et al.*, 2015; Hook *et al.*, 2019; Tang and Cheng, 2019]. The latter has been overwhelmingly used in almost all ABH-based EH-related researches. Despite its universality in coping with structural complexity, FE is seen to be computationally intensive and to lack flexibilities in terms of system optimization. On the contrary, though only applicable to simple structures, energy-based semi-analytical models [Tang *et al.*, 2016] show advantages in capturing basic physical phenomena and performing system optimizations [Ma and Cheng, 2019b]. Efforts were made to improve the modeling efficiency by using different admissible functions [Wang *et al.*, 2019; Deng *et al.*, 2020]. However, up to now, all these existing semi-analytical models are based on Rayleigh–Ritz procedure and adopt Euler–Bernoulli assumptions for beams and Love–Kirchhoff assumptions for plates, which both neglect the shear and rotational effects. These assumptions, though acceptable for investigating the overall dynamics of ABH structures, may lead to significant inaccuracies within the thinnest region of an ABH, for example, the tip region of an ABH beam. As to be demonstrated later, this area happens to be the most critical area for EH, where the structural deformation is large and broadband frequency responses need to be considered. In addition, piezoelectric patches inside the ABH area interact with the host structure, mainly in two ways: generating electromechanical coupling with the host structure which is indispensable for EH and compromising the ABH effects due to the increased structural stiffness which may adversely affect the energy trapping. These compelling factors need to be meticulously considered and balanced during the system design. Obviously, this requires a flexible simulation tool to cope with the specific needs of ABH-based EH to guide the system design. Meanwhile, a good understanding and quantification

of the electromechanical coupling and energy conversion in the system is also of paramount importance to achieve efficient EH.

Motivated by the above, this paper targets a two-fold objective: (a) to propose a semi-analytical electromechanical model which considers the full electromechanical coupling between a host beam and the coated PZT patches and the high-frequency shear effects of the beam and (b) to apply the proposed model to a benchmark PZT-coated ABH beam and carry out systematic analyses on a few important issues pertinent to EH and to explore the underlying mechanisms governing the electromechanical coupling and energy conversion.

The rest of the paper is organized as follows. Theoretical formulation is first presented. The model is then validated through comparisons with experiments and the FE results, alongside a brief discussion on the convergence behavior of the model in terms of the newly added rotational angle of the beam cross-sections. Numerical analyses are then conducted to show typical ABH-specific features as well as the influence of the PZT layout on the electromechanical coupling strength of the system and the corresponding EH efficiency. Results show that ABH effects allow for effective EH upon a proper design of the system and due consideration of the PZT layout in relation to the wavelength and frequency range. To guide the design, some guiding criteria on the deployment of the PZT are established which maximize the ABH benefits and the EH performance.

2. Theoretical Model and Formulation

As shown in Fig. 2, the system under investigation consists of a beam undergoing flexural vibration under a point force excitation $f(t)$ at x_f. The beam, with a constant width b, is composed of a uniform portion with a constant thickness $2h_u$ and an ABH portion with variable power-law profiled thickness ($2h_b$) from x_u to l, i.e., $h_b(x) = \beta(l_{\text{ref}} - x)^m$, in which l_{ref} is a reference length, corresponding to the length of an ABH beam when its terminal thickness reduces to zero, i.e., a beam without truncation. Piezoelectric patches with a constant thickness h_e and a length

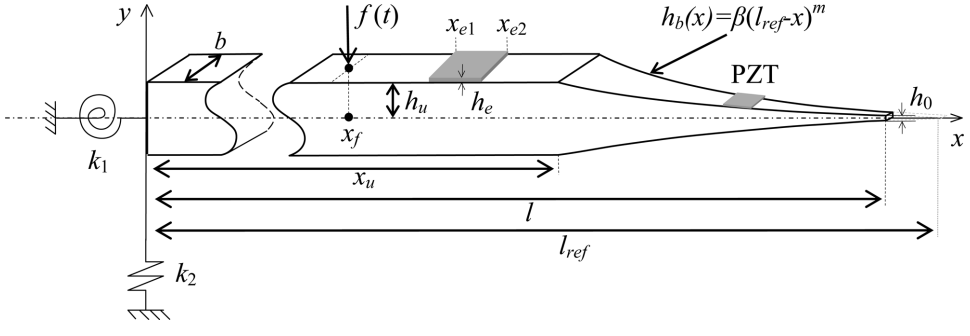

Fig. 2. A Timoshenko beam with symmetrical ABH power-law profiles.

x_e are symmetrically placed over the two surfaces (top and bottom) of the beam from x_{e1} to x_{e2}. The whole system is therefore symmetrical with respect to the mid-line of the beam. The non-uniform end of the beam is free, whereas the other end is elastically supported by a rotational spring k_1 and a translational spring k_2, the stiffness of which can be adjusted to mimic various boundary conditions. For example, by assigning large values to k_1 and k_2 which are sufficiently higher than the overall stiffness of the beam, a clamped boundary can be simulated. Such a treatment also eliminates the geometrical boundary conditions of the system, thus facilitating the choice of the admissible functions to approximate vibration displacement of the system [Tang *et al.*, 2016].

Timoshenko deformation assumption is adopted to accommodate the need of achieving a more accurate characterization of the beam vibration, especially toward its tip area. As such, the cross-sectional rotational inertia and shear deformation of the beam are to be considered. Therefore, the displacement field of the beam can be written as:

$$\{u(x,y,t), w(x,y,t)\} = \left\{-y \cdot \left[\frac{\partial w(x,t)}{\partial x} + \theta(x,t)\right], w(x,t)\right\}, \tag{1}$$

where $u(x,y,t)$ and $w(x,y,t)$ are, respectively, the displacements of an arbitrary point in the beam along the x- and y-axes, and $u(x,t)$ and $w(x,t)$ are the corresponding displacement components in the mid-plane. t is the time. $\theta(x,t)$ is the rotational angle of the beam cross-section. Details are shown in Fig. 3.

The linear strain–displacement relations yield the following normal strain and shear strain expressions:

$$\varepsilon_{xx} = \frac{\partial u(x,y,t)}{\partial x} = -y \cdot \left[\frac{\partial^2 w(x,t)}{\partial x^2} + \frac{\partial \theta(x,t)}{\partial x}\right], \tag{2}$$

$$\gamma_{xy} = \frac{\partial u(x,y,t)}{\partial y} + \frac{\partial w(x,y,t)}{\partial x} = -\theta. \tag{3}$$

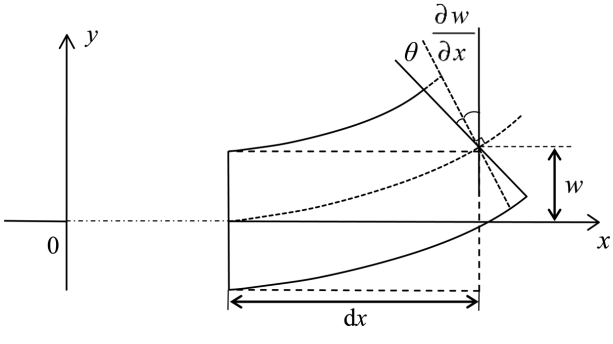

Fig. 3. Illustration on the two system unknowns.

The out-of-plane displacement, $w(x,t)$, and the rotation angle, $\theta(x,t)$, are expressed as:

$$w(x,t) = \sum_{i=0} \varphi_i(x) a_i(t) = \boldsymbol{\varphi}(x)\mathbf{a}(t), \tag{4}$$

$$\theta(x,t) = \sum_{i=0} \phi_i(x) b_i(t) = \boldsymbol{\Phi}(x)\mathbf{b}(t), \tag{5}$$

where $\varphi_i(x)$ and $\phi_i(x)$ are the assumed admissible shape functions for $w(x,t)$ and $\theta(x,t)$, respectively. Encapsulated into vectors, they are contained in $\boldsymbol{\varphi}(x)$ and $\boldsymbol{\Phi}(x)$, respectively. Expressed this way, $a_i(t)$ and $b_i(t)$ are the corresponding temporal coordinates to be determined, also packed into two unknown vectors $\mathbf{a}(t)$ and $\mathbf{b}(t)$, respectively. There are many possible choices for $\varphi_i(x)$ and $\phi_i(x)$ as long as they are linearly independent, since the use of the artificial springs has removed all the geometrical boundary conditions. For convenience, the same admissible functions are used for $\varphi_i(x)$ and $\phi_i(x)$ in the subsequent analyses. More specifically, we adopt a set of modified trigonometric functions with supplementary boundary smoothing terms as follows [Wang *et al.*, 2019]:

$$\begin{aligned} w(x,t) = &\sum_{i=0}^{N} \cos(\lambda_{il}x) a_i(t) + \zeta_{1l}(x) a_{N+1}(t)|_{x=0} + \zeta_{2l}(x) a_{N+2}(t)|_{x=l} \\ &+ \zeta_{3l}(x) a_{N+3}(t)|_{x=0} + \zeta_{4l}(x) a_{N+4}(t)|_{x=l} \end{aligned} \tag{6}$$

$$\begin{aligned} \theta(x,t) = &\sum_{i=0}^{M} \cos(\lambda_{il}x) b_i(t) + \zeta_{1l}(x) b_{M+1}(t)|_{x=0} + \zeta_{2l}(x) b_{M+2}(t)|_{x=l} \\ &+ \zeta_{3l}(x) b_{M+3}(t)|_{x=0} + \zeta_{4l}(x) b_{M+4}(t)|_{x=l}, \end{aligned} \tag{7}$$

where $\lambda_{il} = i\pi/l$, with $i = 0, 1, 2, \ldots$ and N and M denoting the truncated number of terms to be kept in the calculation. Reasons for choosing such functions are briefly recalled as follows. Standard trigonometric series show excellent fitting capability and smoothness, except at the beam boundary. In the present case, they cannot satisfy the elastic boundary conditions of ABH beam due to the differential discontinuities of the higher-order spatial derivatives at the boundaries. As demonstrated earlier for a Euler–Bernoulli beam [Wang *et al.*, 2019], to satisfy the differential continuity requirements by the force equilibrium and geometric coordination at the general elastic end supports, the standard trigonometric series should be supplemented by auxiliary boundary smoothening functions $\zeta(x)$. Detailed expressions of these functions are given in Appendix A, with more details provided in our previous work [Wang *et al.*, 2019]. When M is zero and last four terms are ignored, i.e., without considering the rotation angle, the model degenerates to a Euler–Bernoulli model.

Classical constitutive equations of piezoelectricity write:

$$\begin{cases} T = c^E S - e^{\mathbf{T}} E^e \\ D = eS + \varepsilon^S E^e \end{cases}, \tag{8}$$

where T is the stress; S the strain; D the electric displacement and E^e the electric field. c^E is the elastic stiffness constant of PZT measured at constant electric field and ε^S the dielectric constant measured at constant strain. The term e is the piezoelectric stress constant. In the present model in which thin PZT patches are used, the electric potential across the PZT element writes:

$$E^e = \frac{v(t)}{\psi(y)} = \frac{v(t)}{h_e}, \tag{9}$$

where $\psi(y)$ is the electrical field function in the thickness direction, which is assumed to be constant as h_e, and $v(t)$ is the electrical voltage across the PZT thickness.

The modeling procedure follows the general variational principle framework [Mi *et al.*, 2018]. Upon constructing the Hamiltonian functional, its externalization leads to the Lagrangian equation:

$$\frac{d}{dt}\left(\frac{\partial L}{\partial \dot{q}_i(t)}\right) - \frac{\partial L}{\partial q_i(t)} = 0, \tag{10}$$

where $q_i(t)$ represents $a_i(t)$, $b_i(t)$ and $v(t)$ and the Lagrangian L is expressed as:

$$L = E_k - E_p + W, \tag{11}$$

in which E_k represents the kinetic energy of the entire system (beam and PZT patches); E_p the corresponding potential energy and W the work done by the external force and electrical loading. These physical quantities are, respectively, expressed as:

$$E_k = \frac{1}{2}\int \rho O \left(\frac{\partial w}{\partial t}\right)^2 dx + \frac{1}{2}\int \rho I \left[\frac{\partial}{\partial t}\left(\frac{\partial w}{\partial x}\right) + \frac{\partial \theta}{\partial t}\right]^2 dx, \tag{12}$$

$$E_p = \frac{1}{2}\int EI\left(\frac{\partial^2 w}{\partial x^2} + \frac{\partial \theta}{\partial x}\right)^2 dx + \frac{1}{2}\int \kappa GO\theta^2 dx + \frac{1}{2}k_1\left(\frac{\partial w}{\partial x} + \theta\right)^2\Bigg|_{x=0} + \frac{1}{2}k_2 w^2\Big|_{x=0} - \int E^{\mathbf{T}} D dV_{\mathrm{p}}, \tag{13}$$

$$W = f(t)w(x,t) - v(t)q(t). \tag{14}$$

Note that the integrations cover both the host beam and PZT patches. Therefore, the parameters involved apply to either the beam or PZT patches depending on the integration domain. More specifically in the above expressions, ρ represents the density of structural components (beam or PZT layers depending on the integration interval); E is their elasticity modulus, in which a structural damping is included as $E = E(1 + i\eta)$ with η being the damping loss factor; G is their shear modulus.

Besides, O denotes the cross-sectional area; I the cross-sectional moment of inertia and κ the cross-section shear coefficient, usually taken as 5/6 [Cowper, 1966]. $v(t)$ is the voltage and $q(t)$ the electric charge.

After truncating the decomposition series in Eqs. (4) and (5), applying Eq. (10) leads to the following fully coupled electromechanical equations, written in a matrix form:

$$(\mathbf{M}_{a1} + \mathbf{M}_{a2}) \cdot \ddot{\mathbf{a}}(t) + \mathbf{M}_{b1} \cdot \ddot{\mathbf{b}}(t) + (\mathbf{K}_{a1} + \mathbf{K}_{a2} + \mathbf{K}_{a3}) \cdot \mathbf{a}(t) + (\mathbf{K}_{b1} + \mathbf{K}_{b2}) \cdot \mathbf{b}(t) - \boldsymbol{\Theta}_1 \cdot v(t) = \mathbf{f}(t) \tag{15}$$

$$\mathbf{M}_{b1} \cdot \ddot{\mathbf{a}}(t) + \mathbf{M}_{b2} \cdot \ddot{\mathbf{b}}(t) + (\mathbf{K}_{b1} + \mathbf{K}_{b2}) \cdot \mathbf{a}(t) + (\mathbf{K}_{b3} + \mathbf{K}_{b4} + \mathbf{K}_{b5}) \cdot \mathbf{b}(t) - \boldsymbol{\Theta}_2 \cdot v(t) = 0, \tag{16}$$

$$\boldsymbol{\Theta}_1^{\mathbf{T}} \cdot \mathbf{a}(t) + \boldsymbol{\Theta}_2^{\mathbf{T}} \cdot \mathbf{b}(t) + C_{eq} \cdot v(t) = q(t), \tag{17}$$

where $\mathbf{M}$ and $\mathbf{K}$ with subscripts stand for different components which form the global mass matrix and stiffness matrix. Similarly, Θ is the electromechanical coupling matrix and C_{eq} is the capacitance of the PZT equivalent circuit. T denotes the transpose of a matrix. Details of these matrix components are provided in Appendix B.

The structure can be connected to an external circuit module as part of the whole coupling system, either for EH or control purposes. The electromechanical coupling in the system is ensured via the electrical voltage $v(t)$. For example, a simple LRC oscillating circuit, shown in Fig. 4, can be used, governed by:

$$L_e \cdot \ddot{q}(t) + R \cdot \dot{q}(t) + \frac{1}{C_e} \cdot q(t) = v(t), \tag{18}$$

where C_e is the capacitance; L_e the inductance and R the resistance of the LRC circuit and C_{eq} the equivalence capacitance of the PZT. This equation should be jointly used with Eq. (17).

The model inherits the following salient features. (1) The displacement field assumption (Eqs. (2) and (3)) as well as the kinetic energy E_k and the potential energy E_p apply to the entire system, including the host ABH beam and PZT patches. Therefore, PZT layers are modeled as an integrated part of the system with

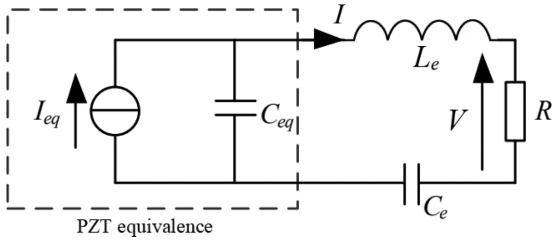

Fig. 4. RLC circuit diagram.

their intrinsic material properties and full coupling with the host beam included into the model. Similarly, should other additional elements be considered, like damping layers, their effects can also be easily added into the system through incorporating their energy terms into the Lagrangian. (2) More relevant to the electromechanical coupling, any external electrical module can also be easily added as part of the system, thus forming a complete set of fully coupled electromechanical models, conducive to studies such as the design of efficient electrical circuits to maximize the EH efficiency or to tactically alter ABH effects of the host structure through electromechanical feedback. (3) In terms of utilization, the above set of coupled equations can be solved in either time or frequency domain. In the latter case, upon a suitable truncation of the decomposition series, both eigen problems or forced vibration problems can be readily solved to obtain the natural frequencies of the system (either open- or short-circuited) or the system response (either mechanical or electrical), respectively.

3. Model Validations with FE Simulations and Experiments

The accuracy of the proposed model is assessed though comparisons with FEM results and experiments. A free-free ABH beam (by assigning $k_1 = k_2 = 0$) is used. The beam configuration is the same as the one used in Tang *et al.* [2016], with its physical and geometrical parameters tabulated in Table 1. The ABH beam is subject to a harmonic point force excitation of 1 N in amplitude at the point $x_f = 0.06$ m on the uniform portion. All calculations are conducted using $N = 146$ and $M = 10$, which ensure converged results within the entire frequency range of interest investigated in this paper (this will be discussed in detail later, and the same set of these parameters will be used in all subsequent analyses). Parameters of a typical piezoelectric ceramic patch PZT-5H [Cheng, 2017] are used in the simulation.

Table 1. Physical and geometrical parameters of the free-free ABH beam.

Material parameters	Geometrical parameters
Beam	Beam
Density: $\rho_b = 7794\,\mathrm{kg/m^3}$	$\beta = 0.125$
Damping loss factor: $\eta_b = 0.005$	$m = 2$ $b = 0.05$ m
Elasticity modulus: $E_b = 200$ GPa	$x_u = 0.16$ m
Shear modulus: $G_b = 97$ GPa	$l = 0.28$ m
	$l_{\mathrm{ref}} = 0.32$ m
PZT	$h_u = 3.2$ mm
Density: $\rho_e = 7600\,\mathrm{kg/m^3}$	$h_0 = 0.4$ mm
Damping loss factor: $\eta_e = 0$	
Elasticity modulus: $E_e = 132$ GPa	*PZT*
Shear modulus: $G_e = 64$ GPa	$x_{e1} = 0.16$ m
Piezoelectric stress constant: $e = -4.1\,\mathrm{C/m^3}$	$x_{e2} = 0.28$ m
Dielectric constant: $\varepsilon^s = 5.84 \times 10^{-9}\,\mathrm{F/m}$	$h_e = 0.4$ mm

3.1. *Validation with FEM results*

The accuracy of the established model is first verified through comparisons with the results of the FEM using COMSOL Multiphysics. The beam and the PZT patches are modeled using *2D Solid Mechanics module* and *Electrical Circuit module*, respectively. For the external electrical circuit, a purely resistive circuit is considered. Non-uniform meshing is used to ensure the accuracy of the FE modeling. The tip region, where the beam thickness reduces to the minimum truncation thickness, is densely meshed by ensuring a minimum of 10 elements per wavelength at the highest frequency of interest. This results in a total of 3316 non-uniform triangular elements. In addition, PZT patches are discretized with 864 triangular elements. The meshing of the structure is shown in Fig. 5, with two insets showing more details on two selected segments of the beam (one at the junction between the uniform portion and the ABH region and the other near the ABH tip).

First, the ABH beam without PZT patches is examined. Table 2 shows a comparison in terms of the first eight resonant frequencies, obtained from different models: FE simulation, Euler–Bernoulli beam and the present model. Relative errors with respect to the FE results are tabulated in the table. It can be seen that both Euler–Bernoulli model or the present model gives reasonably accurate results for the lower order modes up to the fourth or fifth one (with an error less than 1% when compared with FE results). For higher order modes, however, Euler–Bernoulli results

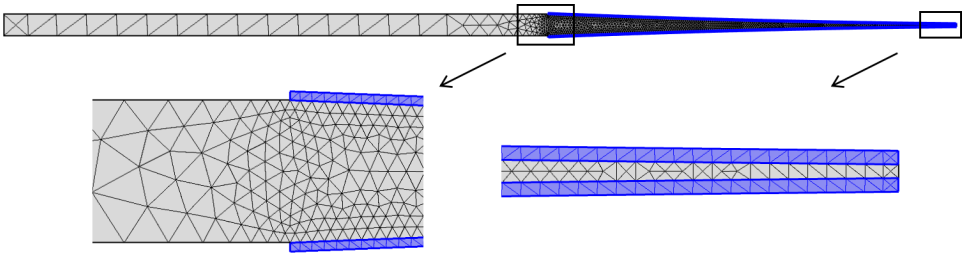

Fig. 5. Details of FE meshing with two sub-insets showing meshing details near two selected segments of the beam (blue color denotes PZT areas).

Table 2. Comparisons of resonant frequencies and relative error with respect to FE results.

FE COMSOL	Euler–Bernoulli		Present model	
Natural frequency	Natural frequency	Error (%)	Natural frequency	Error (%)
448.42	448.73	0.0691	449.22	0.1784
821.07	822.53	0.1778	821.86	0.0962
1452.4	1457.0	0.3167	1454.5	0.1446
2264.7	2278.4	0.6049	2267.1	0.1060
3238.9	3266.4	0.8491	3244.5	0.1729
4461.4	4517.4	1.2552	4469.7	0.1860
5805.8	5904.2	1.6949	5822.5	0.2876
7390.1	7554.6	2.2260	7420.8	0.4154

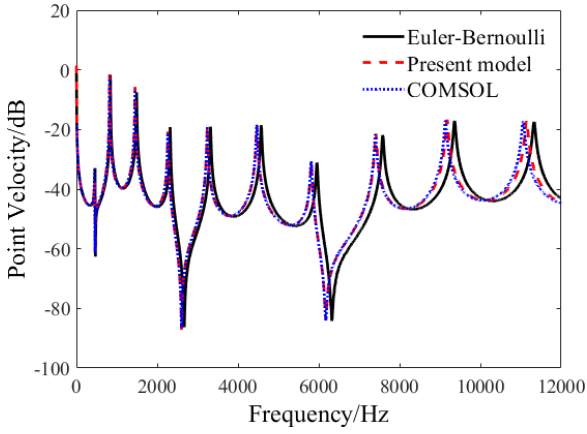

Fig. 6. Comparisons among different models of the point velocity response of a free ABH beam without PZT layers.

start to show obvious error, reaching over 2% for the eighth mode of the beam. Using the present model together with the use of admissible displacement functions, an improved calculation accuracy is achieved (with an error typically capped at roughly 0.4% for all eight modes considered). This verifies the improved accuracy of the established model.

The point velocity response curves from different models are shown in Fig. 6. The point velocity is expressed in terms of decibel (dB, 20 log 10(velocity) referenced to 1). It follows that the result from the present model agrees very well with the FE simulation, in terms of both amplitude and peak locations (the measurement point is $x_m = 0.27\,\mathrm{m}$). The model successfully alleviates the obvious errors produced by the Euler–Bernoulli model in terms of discrepancy of the resonance peak locations, especially at the high frequency end of the curves. It is therefore apparent that the neglected shear and rotational effects in the Euler–Bernoulli model are important in such an ABH beam, and they are indeed well apprehended by the current model through introducing an additional degree of freedom via rotational angle $\theta(x,t)$.

Capitalizing on this configuration, we further investigate the convergence behavior of the present model. While the series truncation rule for the out-of-plane displacement of the beam (N in Eq. (6)) has been well tested and respected in the current calculation to ensure a converged result, the same analysis is performed here for the newly introduced rotational angle (M in Eq. (7)). Using $N = 146$, which ensures the converged solution for the corresponding Euler–Bernoulli beam, Fig. 7 shows the calculated velocity results for different M values. Note $M = 0$ corresponds to Euler–Bernoulli model. It can be seen that, as expected, the calculated resonance peaks are shifted toward low frequency with the increase of M (from 0 to 10) as a result of the rotation- and shear-induced reduction in the structural stiffness. When M continues to increase to 50, however, the curve almost coincides

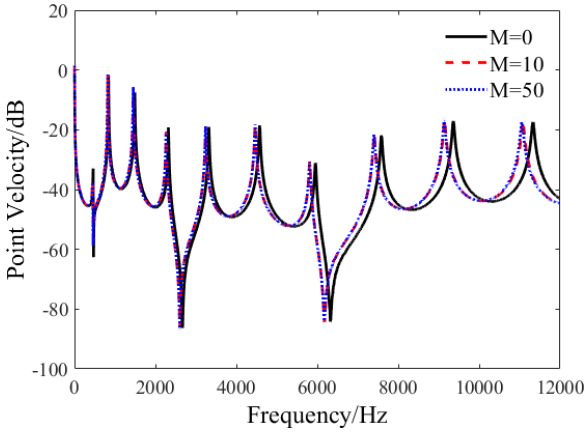

Fig. 7. Convergence with respect to the truncation term M used in rotational angle approximation.

with the one using $M = 10$, thus suggesting that the results have converged. It can also be seen that although the consideration of the shear effect and the rotational angle is important, only a small number of decomposition terms, when compared with the truncation order for the out-of-plane motion, would be enough to ensure the accuracy of the calculation.

With piezoelectric patches added to the beam, using parameters tabulated in Table 1, comparisons with FEM results have also been carried out in terms of both point velocity responses (Fig. 8(a)) and electrical power output from the PZT (Fig. 8(b)). It follows that the present model also agrees very well with the FE results, in terms of both amplitude level and resonance frequencies, as shown in both comparison figures. For the latter, we use a purely resistive circuit conceded

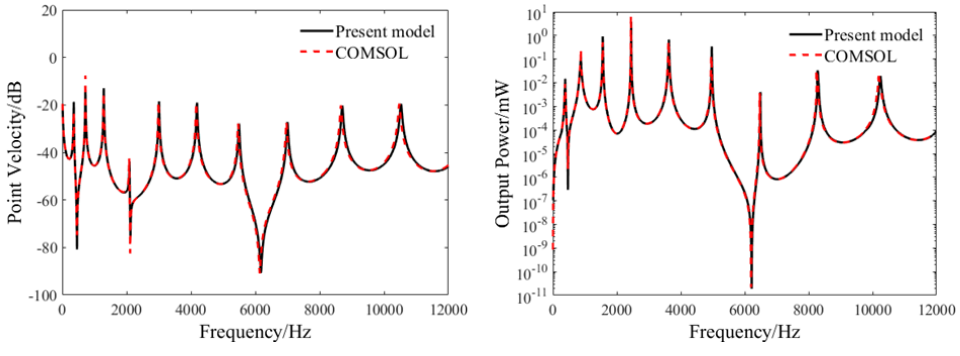

(a) (b)

Fig. 8. Comparisons between different models with PZT on the beam: (a) point velocity and (b) output electrical power.

to the PZT. As a representative example, PZT patches cover the entire ABH portion of the beam. With an electrical resistance $R = 1000\,\Omega$, the harvested electrical power from each PZT patch is calculated as $P = V^2/R$, thus giving the total harvested electrical power of $P_{\text{out}} = 2P$. From Fig. 8(b), it can be seen that the predicted result by the present model is highly consistent with the FE simulations, in terms of both amplitude and peak locations.

3.2. *Experimental validations*

The same ABH beam used in Fig. 6 was experimentally tested. The beam was suspended by two thin strings, which were attached to a rigid frame to produce the free boundary conditions of the beam, as shown in Fig. 9. The beam was excited at a point 0.22 m away from the ABH tip using an electromagnetic shaker with the force measured through a force transducer (B&K 8200) and amplified by a charge amplifier (B&K 2635). A Polytec scanning laser vibrometer (PSV) was used to generate a periodic chirp signal with frequency from 0 Hz to 12 kHz to feed the shaker via a power amplifier (B&K 2706) and to scan the whole beam for response measurement.

Velocities predicted by the present model at a point which is 0.01 m away from the tip of the beam are compared with the experimentally measured results in Fig. 10. It can be seen that, despite some noticeable differences, the general variation tendency of the vibration response with respect to frequencies is reasonably well predicted by the proposed model. Discrepancies, though visible in some resonance peaks as well as in the dip region (around 6400 Hz), are deemed acceptable from engineering viewpoint. This further validates the model.

Therefore, the proposed model, as well as the improvement it brings about to the existing semi-analytical model, has been fully validated from both passive and

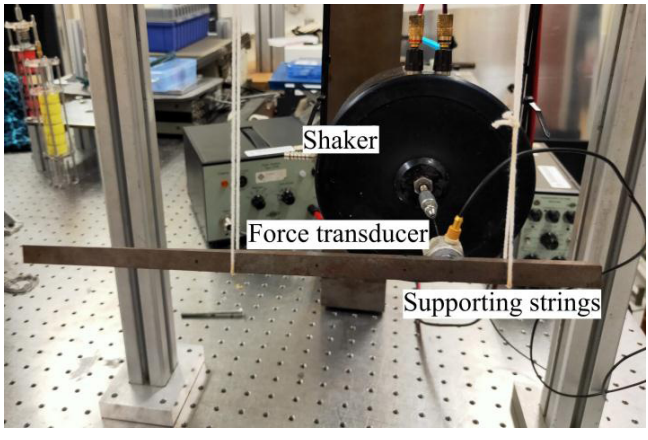

Fig. 9. Experimental set-up.

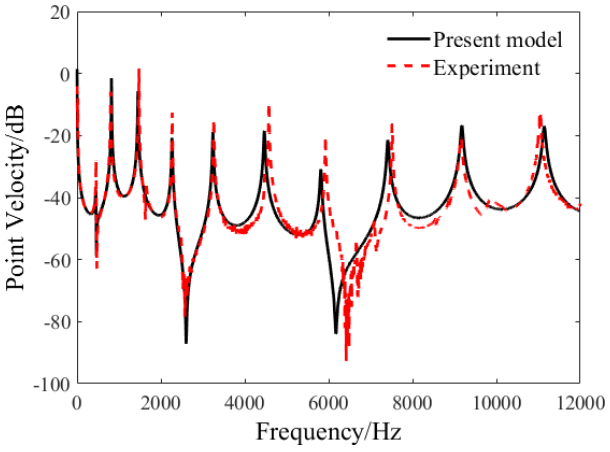

Fig. 10. Comparisons of point velocity response with experiment.

coupled electro-mechanical perspectives. As a side note on the efficacy of the proposed model, its computational efficiency is also roughly estimated against FE simulation. Using the same step size, the present model is roughly five times faster than the FE simulation using COMSOL. Owing to the modular and energy-based nature, the proposed semi-analytical model offers the flexibility and the efficiency as a useful platform for guiding the design and eventually the optimization of an ABH-based EH beam system.

4. Numerical Analyses on ABH-Specific EH and Electromechanical Coupling

Using the established model, issues pertinent to EH are investigated, including the quantification of the EH performance and its relationship with ABH features, influences of the PZT layout and characterization of electromechanical coupling and that of the energy conversion efficiency. The analyses lead to some simple design principles based on the electromechanical coupling coefficient of the structure. The system under investigation is a cantilever ABH beam (clamped at the end of the uniform portion and free at the ABH tip), with physical and geometrical parameters tabulated in Table 3. Parameters marked as case-specific in the table are variables to be defined in each case. The beam is subject to a harmonic point force excitation of 1 N in amplitude at $x_f = 10$ cm on the uniform portion. The clamped boundary is simulated using $k_1 = k_2 = 10^{12}$, by following the established procedure [Cheng and Nicolas, 1992]. In the present case, no meaningful changes are observed when further increasing these values, which means that a converged solution has been obtained. The same values of N and M as in the free boundary case are used in the simulation. The convergence of the calculation was carefully checked in a way similar to the free-beam case.

Table 3. Physical and geometrical parameters of the cantilever ABH beam.

Material parameters	Geometrical parameters
Beam	*Beam*
Density: $\rho_b = 7800\,\mathrm{kg/m^3}$	$\beta = 0.1$
Damping loss factor: $\eta_b = 0.005$	$m = 2$
Elasticity modulus: $E_b = 210\,\mathrm{GPa}$	$b = 0.05\,\mathrm{m}$
Shear modulus: $G_b = 102\,\mathrm{GPa}$	$x_u = 0.25\,\mathrm{m}$
	$l = 0.45\,\mathrm{m}$ (case-specific)
PZT	$l_{\mathrm{ref}} = 0.5\,\mathrm{m}$
Density: $\rho_e = 7600\,\mathrm{kg/m^3}$	$h_u = 6.25\,\mathrm{mm}$
Damping loss factor: $\eta_e = 0$	$h_0 = 0.5\,\mathrm{mm}$ (case-specific)
Elasticity modulus: $E_e = 132\,\mathrm{GPa}$	
Shear modulus: $G_e = 64\,\mathrm{GPa}$	*PZT*
Piezoelectric stress constant: $e = -4.1\,\mathrm{C/m^3}$	$x_{e1} = 0.25\,\mathrm{m}$ (case-specific)
Dielectric constant: $\varepsilon^s = 5.84 \times 10^{-9}\,\mathrm{F/m}$	$x_{e2} = 0.45\,\mathrm{m}$ (case-specific)
	$h_e = 0.5\,\mathrm{mm}$

4.1. *ABH-specific phenomena near the tip region*

Having demonstrated the differences between different beam models in previous sections, the necessity of the proposed model in characterizing ABH-specific physical phenomena is investigated from EH perspective. Meanwhile, a good understanding on system dynamics will also be beneficial for the subsequent EH analyses.

With flexural waves propagating inside the ABH beam, the phase velocity of the waves, c, within the ABH portion is governed by [Tang and Cheng, 2017a]:

$$c = 2\sqrt{\pi f h}\left[\frac{E_b}{12\rho_b}\right]^{\frac{1}{4}}, \tag{19}$$

where h denotes the half-thickness of the beam, applicable to either the uniform portion (h_u) or the ABH portion (h_b). Obviously, c decreases when the thickness h decreases. The corresponding wavelength $\lambda = c/f$ writes

$$\lambda = 2\sqrt{\frac{\pi h}{f}}\left[\frac{E_b}{12\rho_b}\right]^{\frac{1}{4}}. \tag{20}$$

An important metric to characterize the ABH phenomena is the cut-on frequency or the characteristic frequency of an ABH structure, denoted by f_c and defined as:

$$f_c = \frac{2\pi h_u}{l_{\mathrm{ABH}}^2}\sqrt{\frac{E_b}{12\rho_b}}, \tag{21}$$

where l_{ABH} denotes the length of the ABH portion. Approaching this frequency, the wavelength of the incoming wave becomes comparable and shorter than the characteristic dimension of the ABH region. The cut-on frequency is commonly used to roughly signal the ABH cut-on, above which systematic ABH effects can be expected, though below which some ABH features may also appear depending on system dynamics [Tang and Cheng, 2017b], albeit not systematically. In this sense,

this frequency should not be used as an absolute limiting value to demarcate the ABH regions, but rather as an indicator. Obviously, the cut-on frequency depends on the length of the ABH portion, which itself is linked to the truncated tip thickness of the beam. A thinner truncated thickness would in principle warrant better ABH effects, but also put harsher requirement on the accuracy of the model to truthfully depict the wave behaviors toward the ABH tip. To illustrate the issue, Fig. 11 shows the calculated velocity of the ABH beam (without PZTs) with two different truncated residual thicknesses at the tip end: one is the nominal beam configuration with a total beam length of 45 cm (with a truncated residual thickness of $h_0 = 0.5$ mm), whereas the other one, 5 cm longer, has no truncation ($h_0 = 0$ mm). The calculated response point remains the same in both cases at $x_m = 45$ cm, which is the tip point of the shorter beam. The figure also shows the comparison between Euler–Bernoulli model and the present model in the case of shorter beam.

Comparisons in Fig. 11 show several typical ABH phenomena which are worth noting. First, the extension of the beam by 5 cm, alongside the elimination of the residual truncated thickness, brings about two eminent phenomena: (a) the number of resonance peaks is significantly increased. Therefore, the structure exhibits increased dynamics and (b) the vibration level at the calculation position is also significantly reduced. Both observations can be attributed to the ABH effects. In fact, by increasing the length of the ABH portion, the cut-on frequency of the beam is reduced, from 1470 Hz down to 940 Hz in the present case. As a result, in addition to the expected low-frequency shift in the natural frequencies of the overall beam due to the length elongation, additional local resonances also increase the number of peaks as the result of an earlier onset of the ABH effects. Most importantly, the slight elongation of the ABH tip also creates a drastic change in the vibration level at the calculation point on the structure. With the extension of the ABH tip

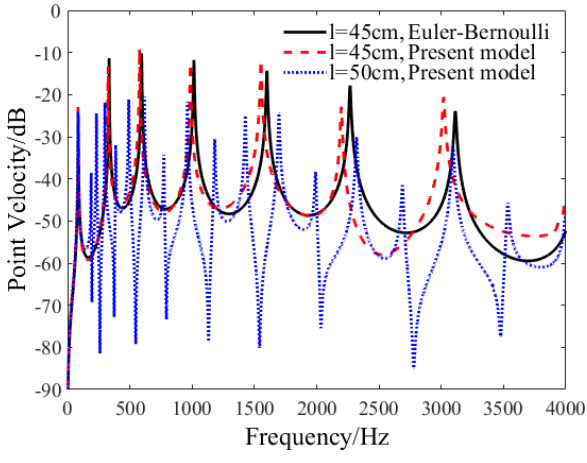

Fig. 11. Point velocities of two ABH beams with/without thickness truncation at $x_m = 45$ cm.

region, the focal location for energy focussing is shifted from $x = 45\,\text{cm}$ (the tip of the shorter beam) to $x = 50\,\text{cm}$ (the tip of the longer beam). This explains why the energy level of the longer beam at $x_m = 45\,\text{cm}$ experiences a drastic reduction when compared with the shorter beam at the same calculation point. The above observation provides additional evidence that the structural dynamics of the ABH structure around the tip region is very complex and sensitive to structural details, thereby posing harsh requirement on the accuracy of the model. Even for the shorter beam, comparisons between the two beam models, depicted in Fig. 11, clearly show the deficiency of the Euler–Bernoulli model, with a much larger discrepancy than what was observed in Fig. 6 in terms of both peak location and level, the reason being the present beam is longer and the observation point is closer to the tip region.

4.2. *EH performance and efficiency*

For the ABH beam under investigation, the EH performance depends on many system parameters including structural details, external EH harvesting circuit as well as parameters related to PZT and its deployment layout over the beam. With no intention to achieve an optimal configuration, we shall focus on a few important issues to illustrate some important and generic aspects relevant to the general ABH-based EH.

As an important EH evaluation metric, apart from the harvested electrical power, we introduce an energy conversion rate, δ, which is defined as the ratio between the harvested electrical power and the input mechanical power:

$$\delta = \frac{P_{\text{out}}}{P_{\text{in}}} = \frac{P_{\text{out}}}{1/2Re\{F \cdot v^*\}}. \tag{22}$$

Note that, based on energy conservation, P_{in} would include both the harvested electrical power and the dissipated power in the mechanical system.

4.2.1. *Effects of the external EH circuit*

Using the PZT configuration tabulated in Table 3, we first examine the effect of an external electrical circuit on EH performance in order to set the ground for subsequent analyses. The external circuit in this case is purely resistant, with a resistance value taken as 100, 1000 and 10,000 Ω, respectively. The results of output power and the energy conversion rate are shown in Figs. 12(a) and 12(b), respectively.

Both figures show that the resistance significantly affects both the output power and energy conversion rate. For the harvested electrical power, different resistances do not seem to affect the position of the peaks which correspond to the system resonances. This partially reflects the weak feedback loading of the external electrical resistance on the vibrating structure. However, they seriously affect the level of the harvested power. Apparently, the influence is also frequency-dependent, and an optimal resistance value only applies to a given frequency range, which can be determined through an optimization problem. The influence of the resistance can

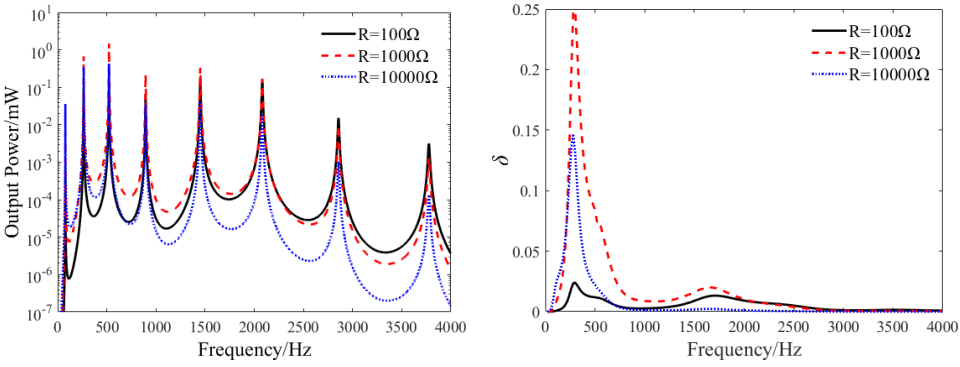

(a) (b)

Fig. 12. Comparison of the EH efficiency with different resistance values.

be better seen by examining the variation of the energy conversion rate, as shown in Fig. 12(b). In the present case, $R = 1000\,\Omega$ seems to provide an acceptable compromise to cover the frequency of interest. As mentioned before, the optimal design of the EH circuit to target particular system configuration is definitely not the focus of this work. Therefore, $R = 1000\,\Omega$ will be used in all subsequent analyses.

4.2.2. *PZT layout and advantages of the ABH-based EH*

The way that PZT is deployed over the vibrating beam will definitely affect the EH power. In order to illustrate this, we will first discuss the effect of PZT position over an ABH beam on the EH efficiency. To demonstrate the benefit that one can draw from the wave-focusing effect in ABH region for EH, the harvested electrical power by the PZTs placed on the free end of the ABH portion is compared with the one when they are placed at the clamped end, which is known as the best position for EH in a cantilever, where the strain energy is the maximum. Another position around the junction between the uniform and ABH portions is also included for comparisons. In all cases, the length of PZT patches is 5 cm, and the external circuit is a pure resistor with $1000\,\Omega$. The output power and the energy conversion rate of the piezoelectric patches corresponding to the three positions are shown in Figs. 13(a) and 13(b), respectively.

By comparing the output power of the three positions (Fig. 13(a)), we can immediately conclude that Position No. 2 shows no advantages over No. 1, while both being placed over the uniform part of the beam. This indeed confirms the common belief that placing PZTs toward the clamped end of a cantilever is indeed desirable in terms of getting a higher energy. Comparing Position No. 1 with Position No. 3 shows that the harvesting at the clamped end seems to deliver higher output power at the very low frequency end. It then becomes comparable with that provided by Position No. 3 before entering into a wide frequency range in which EH at the end of the ABH tip region (No. 3) outperforms the clamped end. This transition roughly

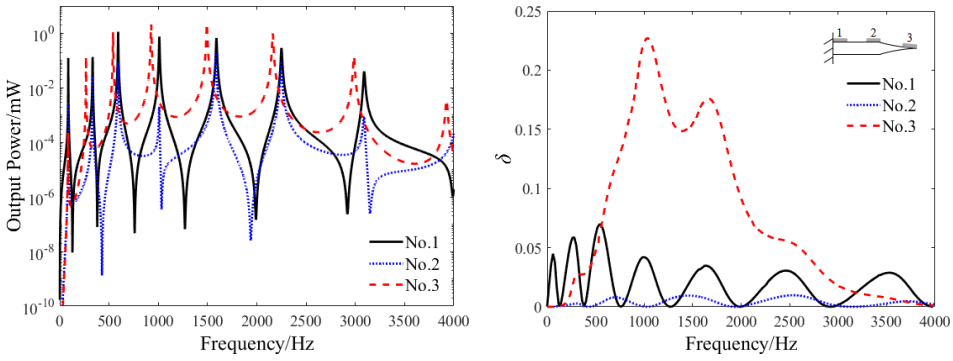

(a) (b)

Fig. 13. Comparison of EH efficiency between different positions.

starts when approaching the cut-on frequency of the ABH beam and definitely in a consistent manner after (1470 Hz). This is definitely owing to the energy trapping effects of the ABH, thus drawing energy away from the rest of the structure to create a high energy concentration around the tip region and pick up by the PZTs. The observed tendency is confirmed from the perspective of the energy conversion rate δ (Fig. 13(b)). Again, the advantage of harvesting energy around the ABH tip region is obvious, consistent with the conclusion drawn from the output power.

On the one hand, EH at the clamped end of ABH beam offers generally lower, but more evenly distributed δ across the entire frequency range. On the other hand, EH at the ABH tip region exhibits very high energy conversion rate over an appreciable broad frequency range after the ABH effect is cut-on, which shows the great potential of the ABH-based broadband EH, including high-frequency energy conversion. It is relevant to note and comment on the observed decreasing trend of δ at the high frequency region, as shown in Fig. 13(b). As will be demonstrated later, the PZT length used in the present example is definitely not optimal for this high frequency band, since the PZT length in this case starts to exceed the half-wavelength of the bending wave. Therefore, the electrical charges produced over different parts of the PZT start to partially neutralize the total energy output. Therefore, a proper sizing of the PZT is expected to offer the ability of tactically targeting particular frequency range in order to achieve the ultimate EH performance.

4.2.3. *Effect of the PZT size*

The size of the PZT patches is an important parameter which should be properly designed for effective EH. The issue is investigated here using the above ABH beam with PZTs of different lengths at the tip region. Note that, in the present case, the shortest wavelength of the bending waves inside the beam occurs at the truncated tip. For the highest frequency considered here, i.e., 4000 Hz, this value is roughly 5 cm. Four lengths of piezoelectric patches are chosen as 20, 5, 2.5 and 1 cm,

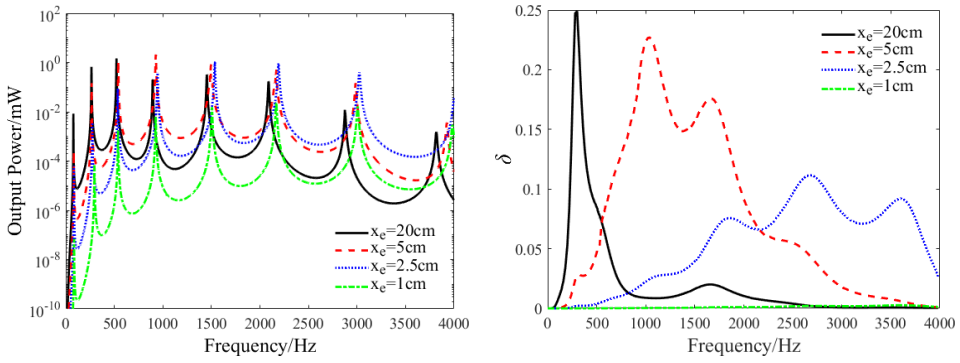

(a) (b)

Fig. 14. Comparison of EH efficiency between different PZT lengths.

respectively. Using the same resistive circuit with $R = 1000\,\Omega$, the harvested electrical power and the energy conversion rate corresponding to the four PZT lengths are shown in Figs. 14(a) and 14(b), respectively.

Figure 14(a) shows that, at low frequencies, exemplified by the first and second peaks, the harvested energy by the longest PZT is obviously the highest. This is understandable, since this low frequency region is dominated by the global modes of the beam, exhibiting long wavelength and overall structural deformation. Therefore, ABH effect is absent in this frequency region and a longer PZT would definitely be beneficial to EH. With the increase of the frequency, shorter PZTs (5 cm and 2.5 cm) start to show better performance when approaching the cut-on frequency of the ABH and the effect is persistent when frequency further increases. This is due to the ABH-induced energy focussing in the ABH portion. A closer examination and comparison between the two curves (corresponding to 5 cm and 2.5 cm) show a transition in terms of the harvested power with the increase of the frequency. More specifically, when compared with the 2.5 cm PZTs, the 5 cm one performs better at first, but deteriorates when frequency increases. This can also be physically explained. In fact, structural wavelength decreases with the frequency, more drastically within the ABH region (Eq. (20)). Therefore, when frequency increases, a longer PZT is more likely to cover more wave undulations, thus producing opposite charges over different parts of the PZT, which ultimately would neutralize the energy output. This, of course, depends on the targeted frequency range. For example, in the present case below 4000 Hz, the shortest PZTs (1 cm) can hardly deliver satisfactory EH performance. The relationship between the optimal PZT length and the structural wavelength will be scrutinized later.

The effective EH frequency range for each PZT length can be better seen in terms of the energy conversion rate (Fig. 14(b)). The observation is basically consistent with the conclusions drawn from the previous power analysis. Definitely, the longest PZTs show high but very narrow effective frequency range, before the

ABH cut-on. With a proper sizing of the PZTs, relatively broadband EH can be achieved after the ABH cut-on, exemplified by the two intermediate length cases investigated here. Though broadband, the frequency zone allowing the highest EH performance, however, depends on the PZT length. Up to a certain limit, a shorter PZT would favor higher frequency EH. Nevertheless, over-shortened PZTs, placed at the tip region of the beam, seem to provide reasonable EH performance, unless the truncation tip becomes very thin and the targeted frequency is extremely high.

Therefore, we can make a preliminary conjecture that the length of the piezoelectric patches should be positively related to the wavelength at the laying position. Different lengths of piezoelectric patches would suit different frequency ranges. With a proper sizing and positioning of the PZT layout, ABH structures can enable efficient, broadband and high frequency EH.

In order to provide a design guideline on the optimal PZT length, the relationship between the PZT length and the structural wavelength in the ABH beam is investigated. To this end, we introduce a dimensionless parameter, referred to as normalized PZT length, x_e/λ_c, where x_e is the length of PZT patch and λ_c is the wavelength of the structure at the center point of the PZT patch. Using this normalized parameter, the energy conversion rate δ, with the same set of PZT lengths, is plotted in Fig. 15. Note due to the truncation thickness of the ABH beam, the range of x_e/λ_c that each PZT length can cover is different. It can be seen from Fig. 15 that, despite the differences in their physical length, the regions corresponding to a high energy conversion rate are all close to, but slightly higher than, $x_e/\lambda_c = 0.5$ i.e., when the PZT length is about half of the wavelength at the central point of the PZT. Though experimentally observed in a previous work on a specific configuration [Ji *et al.*, 2019a], results from Fig. 15 confirm this rather general relationship between the structural wavelength and the laying size of the piezoelectric patches quantitatively, which offers a rule of thumb and useful guidance for determining

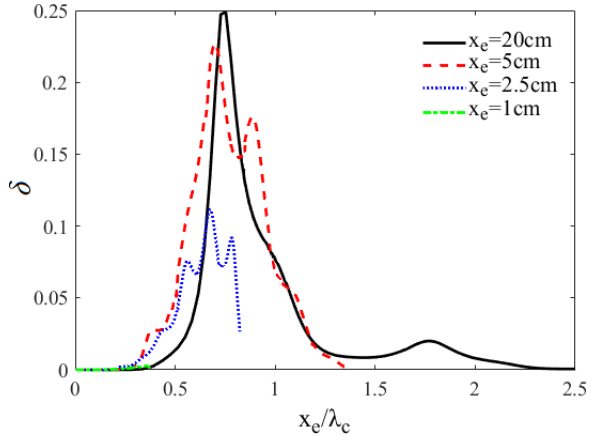

Fig. 15. Energy conversion rates with respect to the normalized PZT length.

the optimal size of the PZT with respect to the operating frequency of the structure as well as the position of the PZT coverage. The observed phenomenon can be explained from the viewpoint of spatial matching between the PZT length and the corresponding structural wavelength. In fact, if the beam were uniform, the optimal normalized PZT length would have been exactly 0.5. For the ABH beam, structural wavelength under the PZT gradually reduces, more significantly toward the tip. Therefore, this ABH-induced wave compression causes the derivation of the optimal normalized PZT length from 0.5. A straightforward extension of this observation would guide the design of multiple PZT patches, in which case multiple PZT patches with different lengths can be deployed to accommodate different parts of the beam to collectively achieve enhanced EH performance.

4.3. *Electromechanical coupling and energy conversion*

Through the above analyses, we understand that numerous parameters would affect the EH efficiency of the ABH-based EH. Therefore, the design of an effective system is a complex problem which should take all these factors into consideration to draw the maximum benefit out of them. The key is to achieve a good understanding and quantification of the electromechanical coupling and the role it plays in the energy conversion process. To guide the design, we examine possible criteria governing the deployment of the PZT to maximize the ABH benefits and the EH performance. To this end, we use the electromechanical coupling factor k to establish its possible relationship with the energy conversion rate. More specifically, k is defined as [Raze *et al.*, 2019]:

$$k^2 = \frac{\omega_{\text{oc}}^2 - \omega_{\text{sc}}^2}{\omega_{\text{sc}}^2}, \tag{23}$$

where ω_{oc} and ω_{sc} are the angular natural frequencies of each mode of the structure when the piezoelectric transducer is open-circuited and short-circuited, respectively. Both can be calculated using the established model by solving the corresponding eigenvalue problems.

Using the same set of configurations as Fig. 15, the electromechanical coupling coefficients k and energy conversion rates δ corresponding to three PZT lengths are computed and shown in Fig. 16. k and δ are shown on the left- and right-hand side axes, respectively. It can be seen that the variations in both k and δ with respect to frequency exhibit very consistent trend in all three cases, thus suggesting that the electromechanical coupling coefficient k could be regarded as a simple and intrinsic indicator of the EH efficiency. It can then be used in the design of effective ABH-based EH structure by tuning or optimizing the numerous physical and geometrical parameters of its components through maximizing k. Note this electromechanical coupling coefficient can either be calculated using the present model or even experimentally measured.

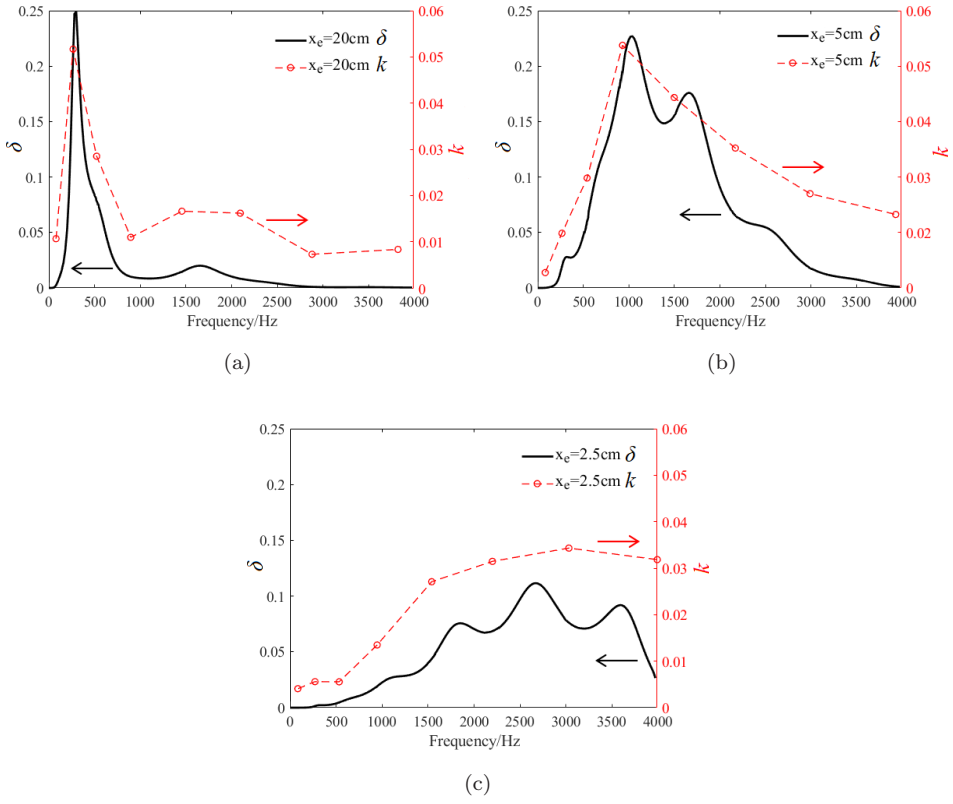

Fig. 16. Comparison of energy conversion rate and electromechanical coupling factor.

5. Conclusions

In this paper, a fully coupled electromechanical model of PZT-coated ABH beams is established. The proposed model considers the full coupling among various electromechanical constituents present in the system. Comparisons with experimental and FE results demonstrate the validity of the model and its improved accuracy in comparison with the existing semi-analytical model. Meanwhile, the necessity of considering the shear and rotational effects of the beam is demonstrated to cope with the ABH beam which features obvious wave compression phenomenon and exhibits complex dynamics within the ABH area, critical to EH applications.

Numerical results show that ABH effects entail effective EH upon a proper design with due consideration of the PZT layout in relation to the wavelength and the targeted frequency range. The unique wave retarding and energy focussing features of the ABH beam favor the PZT installation in the vicinity of its tip area, which warrants better EH performance than the common practice of harvesting at the clamped end, within a broad frequency range except the very low end before the ABH cut-on. Approaching and above the ABH cut-on, upon a proper sizing

of the PZT, ABH offers efficient and broadband EH, as reflected by the enhanced harvested power and energy conversion rate.

While the tip region proves to be an ideal area for PZT installation, its dimension however needs to be meticulously designed to cope with the targeted frequency range. Numerical results show that, in general, a shorter PZT would favor higher frequency EH. As a rule of thumb, a PZT should be sized in such a way that, for a given frequency/frequency range, the normalized PZT length (with respect to the structural wavelength at the center of the PZT-covered region) is close, but slightly larger than 0.5 to ensure a high energy conversion rate. Should one need a more rigorous design criterion? The electromechanical coupling is shown to exhibit consistent variations with the energy conversion rate of the system, thus providing a good indicator to be used for either evaluating the EH performance or tuning/optimizing system parameters for enhanced EH performance.

As a final remark, it is relevant to note that this work puts its emphasis on some fundamental issues pertinent to ABH-based EH from the perspective of simulation model and the underlying physics. Though definitely possible, no effort has been made to strive for optimal EH performance which is configuration-specific and requires system optimization. This, if necessary, can be readily done using the proposed simulation model, which goes beyond the main scope of this paper. Meanwhile, the extension of the proposed model to plate structures should not pose particular technical difficulties. Cases like ABH plates embedded with circular ABH indentations without PZTs have previously been investigated both numerically under Love–Kirchhoff deformation assumptions [Ma and Cheng, 2019a] and experimentally [Ma and Cheng, 2020]. Since the proposed modeling framework is energy-based, the addition of PZTs and external electrical circuits should also be straightforward by following the same procedure established in the present paper.

Acknowledgment

The authors thank the support from the Research Grant Council of the Hong Kong SAR (PolyU 152023/20E) and National Science Foundation of China (No. 11532006).

Appendix A. Formulas of Auxiliary Boundary Smoothening Functions $\zeta(x)$

$$\zeta_{1l}(x) = \frac{9l}{4\pi}\sin\left(\frac{\pi x}{2l}\right) - \frac{l}{12\pi}\sin\left(\frac{3\pi x}{2l}\right)$$

$$\zeta_{1l}(0) = 0, \quad \zeta'_{1l}(0) = 1, \quad \zeta''_{1l}(0) = 0, \quad \zeta_{1l}(l) = \frac{7l}{3\pi}, \quad \zeta'_{1l}(l) = 0, \quad \zeta''_{1l}(l) = -\frac{3\pi}{4l}$$

$$\zeta_{2l}(x) = -\frac{9l}{4\pi}\cos\left(\frac{\pi x}{2l}\right) - \frac{l}{12\pi}\cos\left(\frac{3\pi x}{2l}\right)$$

$$\zeta_{2l}(0) = -\frac{7l}{3\pi}, \quad \zeta'_{2l}(0) = 0, \quad \zeta''_{2l}(0) = \frac{3\pi}{4l}, \quad \zeta_{2l}(l) = 0, \quad \zeta'_{2l}(l) = 1, \quad \zeta''_{2l}(l) = 0$$

$$\zeta_{3l}(x) = \frac{l^3}{\pi^3}\sin\left(\frac{\pi x}{2l}\right) - \frac{l^3}{3\pi^3}\sin\left(\frac{3\pi x}{2l}\right)$$

$$\zeta_{3l}(0) = 0, \quad \zeta'_{3l}(0) = 0, \quad \zeta''_{3l}(0) = 0, \quad \zeta_{3l}(l) = \frac{4l^3}{3\pi^3}, \quad \zeta'_{3l}(l) = 0, \quad \zeta''_{3l}(l) = -\frac{l}{\pi}$$

$$\zeta_{4l}(x) = -\frac{l^3}{\pi^3}\cos\left(\frac{\pi x}{2l}\right) - \frac{l^3}{3\pi^3}\cos\left(\frac{3\pi x}{2l}\right)$$

$$\zeta_{4l}(0) = \frac{4l^3}{3\pi^3}, \quad \zeta'_{4l}(0) = 0, \quad \zeta''_{4l}(0) = \frac{l}{\pi}, \quad \zeta_{4l}(l) = 0, \quad \zeta'_{4l}(l) = 0, \quad \zeta''_{4l}(l) = 0$$

Appendix B. Formulas of Different Terms in Matrices Used in Eq. (17)

Formulas for various terms involved in the mass matrix $\mathbf{M}$ are detailed as follows:

$$\mathbf{M}_{a1} = 2\rho b \int h\boldsymbol{\varphi}^{\mathbf{T}}(x)\boldsymbol{\varphi}(x)dx,$$

$$\mathbf{M}_{a2} = \frac{2}{3}\rho b \int h^3\boldsymbol{\varphi}^{\mathbf{T}}(x)'\boldsymbol{\varphi}(x)'dx,$$

$$\mathbf{M}_{b1} = \frac{2}{3}\rho b \int h^3\boldsymbol{\varphi}^{\mathbf{T}}(x)'\boldsymbol{\Phi}(x)dx,$$

$$\mathbf{M}_{b2} = \frac{2}{3}\rho b \int h^3\boldsymbol{\Phi}^{\boldsymbol{T}}(x)\boldsymbol{\Phi}(x)dx.$$

Formulas for various terms involved in the mass matrix $\mathbf{K}$ are:

$$\mathbf{K}_{a1} = \frac{2}{3}Eb \int h^3\boldsymbol{\varphi}^{\mathbf{T}}(x)''\boldsymbol{\varphi}(x)''dx,$$

$$\mathbf{K}_{a2} = k_1\boldsymbol{\varphi}^{\mathbf{T}}(x)'|_{x=0}\boldsymbol{\varphi}(x)'|_{x=0},$$

$$\mathbf{K}_{a3} = k_2\boldsymbol{\varphi}^{\mathbf{T}}(x)|_{x=0}\boldsymbol{\varphi}(x)|_{x=0},$$

$$\mathbf{K}_{b1} = \frac{2}{3}Eb \int h^3\boldsymbol{\varphi}^{\mathbf{T}}(x)''\boldsymbol{\Phi}(x)'dx,$$

$$\mathbf{K}_{b2} = k_1\boldsymbol{\varphi}^{\mathbf{T}}(x)'|_{x=0}\boldsymbol{\Phi}(x)|_{x=0},$$

$$\mathbf{K}_{b3} = \frac{2}{3}Eb \int h^3\boldsymbol{\Phi}^{\mathbf{T}}(x)'\boldsymbol{\Phi}(x)'dx,$$

$$\mathbf{K}_{b4} = 2\kappa Gb \int h\boldsymbol{\Phi}^{\mathbf{T}}(x)\boldsymbol{\Phi}(x)dx,$$

$$\mathbf{K}_{b5} = k_1\boldsymbol{\Phi}^{\mathbf{T}}(x)|_{x=0}\boldsymbol{\Phi}(x)|_{x=0}.$$

Formulas for the electromechanical coupling matrix Θ are:

$$\boldsymbol{\Theta}_1 = -e^{\mathbf{T}} b \int_{x_{e1}}^{x_{e2}} \left[h_b(x) + \frac{1}{2} h_e \right] \boldsymbol{\varphi}^{\mathbf{T}}(x)'' dx,$$

$$\boldsymbol{\Theta}_2 = -e^{\mathbf{T}} b \int_{x_{e1}}^{x_{e2}} \left[h_b(x) + \frac{1}{2} h_e \right] \boldsymbol{\Phi}^{\mathbf{T}}(x)' dx.$$

The equivalent capacitance of PZT is:

$$C_{eq} = \varepsilon^S b \frac{1}{h_e} (x_{e2} - x_{e1}).$$

The force vector $\mathbf{F}$ is

$$\mathbf{F} = F \boldsymbol{\varphi}^{\mathbf{T}}(x).$$

References

Aklouche, O., Pelat, A., Maugeais, S. and Gautier, F. [2016] "Scattering of flexural waves by a pit of quadratic profile inserted in an infinite thin plate," *Journal of Sound and Vibration* **375**, 38–52.

Bowyer, E. P. and Krylov, V. V. [2015] "Experimental study of sound radiation by plates containing circular indentations of power-law profile," *Applied Acoustics* **88**, 30–37.

Cheng, L. and Nicolas, J. [1992] "Free vibration analysis of a cylindrical shell circular plate system with general coupling and various boundary conditions," *Journal of Sound and Vibration* **155**, 231–247.

Cheng, Z. [2017] "Theories and methods of piezoelectric vibration energy harvesting," *National Defense Industry Press* **1**, 61.

Chong, B. M. P., Tan, L. B., Lim, K. M. and Lee, P. H. [2017] "A review on acoustic black-holes (ABH) and the experimental and numerical study of ABH-featured 3D printed beams," *International Journal of Applied Mechanics* **9**(6), 1750078.

Conlon, S. C. and Feurtado, P. A. [2018] "Progressive phase trends in plates with embedded acoustic black holes," *Journal of Acoustical Society of America* **143**(2), 921–930.

Conlon, S. C., Fahnline, J. B. and Semperlotti, F. [2015] "Numerical analysis of the vibroacoustic properties of plates with embedded grids of acoustic black holes," *Journal of the Acoustical Society of America* **137**(1), 447–457.

Cowper, G. R. [1966] "The shear coefficient in Timoshenko's beam theory," *Journal of Applied Mechanics* **33**(2), 335–340.

Deng, J., Guasch, O. and Zheng, L. [2020] "A semi-analytical method for characterizing vibrations in circular beams with embedded acoustic black holes," *Journal of Sound and Vibration* **476**, 115307.

Denis, V., Pelat, A., Gautier, F. and Elie, B. [2014] "Modal overlap factor of a beam with an acoustic black hole termination," *Journal of Sound and Vibration* **333**, 2475–2488.

Feurtado, F. A. and Conlon, S. C. [2017] "Transmission loss of plates with embedded acoustic black holes," *The Journal of the Acoustical Society of America* **142**, 1390–1398.

Hook, K., Cheer, J. and Daley, S. [2019] "A parametric study of an acoustic black hole on a beam," *Journal of Acoustical Society of America* **145**(6), 3488–3498.

Ji, H., Liang, Y., Qiu, J., Cheng, L. and Wu, Y. [2019a] "Enhancement of vibration based energy harvesting using compound acoustic black holes," *Mechanical Systems and Signal Processing* **132**, 441–456.

Ji, H., Wang, X., Qiu, J., Cheng, L., Wu, Y. and Zhang, C. [2019b] "Noise reduction inside a cavity coupled to a flexible plate with embedded 2-d acoustic black holes," *Journal of Sound and Vibration* **455**, 324–338.

Kralovic, V. and Krylov, V. V. [2007] "Damping of flexural vibrations in tapered rods of power-law profile: Experimental studies," *Proceeding of the Institute of Acoustics* **29**, 66–73.

Krylov, V. V. [1989] "Conditions for validity of the geometrical-acoustics approximation in application to waves in an acute-angle solid wedge," *Soviet Physics-Acoustics* **35**, 176–180.

Krylov, V. V. [1998] "On the velocities of localized vibration modes in immersed solid wedges," *Journal of Acoustical Society of America* **103**, 767–770.

Krylov, V. V. [2004] "New type of vibration dampers utilising the effect of acoustic black holes," *Acta Acustica United Acustica* **90**(5), 830–837.

Lee, J. Y. and Jeon, W. [2017] "Vibration damping using a spiral acoustic black hole," *The Journal of the Acoustical Society of America* **141**(3), 1437–1445.

Leng, F., Romero-García, V., Pelat, A., Picó, R., Groby, J. P. and Gautier, F. [2020] "Interpretation of the acoustic black hole effect based on the concept of critical coupling," *Journal of Sound and Vibration* **471**, 115199.

Li, X. and Ding, Q. [2019] "Sound radiation of a beam with a wedge-shaped edge embedding acoustic black hole feature," *Journal of Sound and Vibration* **439**, 287–299.

Ma, L. and Cheng, L. [2019a] "Sound radiation and transonic boundaries of a plate with an acoustic black hole," *Journal of Acoustical Society of America* **145**, 164–172.

Ma, L. and Cheng, L. [2019b] "Topological optimization of damping layout for minimized sound radiation of an acoustic black hole plate," *Journal of Sound and Vibration* **458**, 349–364.

Ma, L. and Cheng, L. [2020] "Numerical and experimental benchmark solutions on vibration and sound radiation of an acoustic black hole plate," *Applied Acoustics* **163**, 107223.

Maugan, F., Chesne, S., Monteil, M., Collet, M. and Yi, K. [2019] "Enhancement of energy harvesting using acoustical-black-hole-inspired wave traps," *Smart Materials and Structures* **28**, 075015.

Mi, Y., Zheng, H., Shen, Y. and Huang, Y. [2018] "A weak formulation for isogeometric analysis of vibro-acoustic systems with non-conforming interfaces," *International Journal of Applied Mechanics* **10**(7), 1850073.

Mironov, M. A. [1988] "Propagation of a flexural wave in a plate whose thickness decreases smoothly to zero in a finite interval," *Soviet Physics-Acoustics* **34**, 318–319.

O'Boy, D. J. and Krylov, V. V. [2011] "Damping of flexural vibrations in circular plates with tapered central holes," *Journal of Sound and Vibration* **330**, 2220–2236.

Ouisse, M., Renault, D., Butaud, P. and Sadoulet-Reboul, E. [2019] "Damping control for improvement of acoustic black hole effect," *Journal of Sound and Vibration* **454**, 63–72.

Pelat, A., Gautier, F., Conlon, S. C. and Semperlotti, F. [2020] "The acoustic black hole: A review of theory and applications," *Journal of Sound and Vibration* **476**, 115316.

Raze, G., Jadoul, A., Guichaux, S., Broun, V. and Kerschen, G. [2019] "A digital nonlinear piezoelectric tuned vibration absorber," *Smart Materials and Structures* **29**, 015007.

Safaei, M., Sodano, H. A. and Anton, S. R. [2019] "A review of energy harvesting using piezoelectric materials: State-of-the-art a decade later (2008-2018)," *Smart Materials and Structures* **28**, 113001.

Solovyev, A. N. and Duong, L. V. [2016] "Optimization for the harvesting structure of the piezoelectric bimorph energy harvesters circular plate by reduced order finite element analysis," *International Journal of Applied Mechanics* **8**(3), 1650029.

Tang, L. and Cheng, L. [2017a] "Enhanced acoustic black effect in beams with a modified thickness profile and extended platform," *Journal of Sound and Vibration* **391**, 116–126.

Tang, L. and Cheng, L. [2017b] "Broadband locally resonant band gaps in periodic beam structures with embedded acoustic black holes," *Journal of Applied Physics* **121**, 194901.

Tang, L. and Cheng, L. [2017c] "Ultrawide band gaps in beams with double-leaf acoustic black hole indentations," *Journal of Acoustical Society of America* **142**(5), 2802–2807.

Tang, L. and Cheng, L. [2019] "Periodic plates with tunneled acoustic-black-holes for directional band gap generation," *Mechanical Systems and Signal Processing* **133**, 106257.

Tang, L., Zhang, S., Ji, H., Cheng, L. and Qiu, J. [2016] "Characterization of acoustic black hole effect using a 1-D fully-coupled and wavelet-decomposed semi-analytical model," *Journal of Sound and Vibration* **374**, 172–184.

Wang, Y., Du, J. and Cheng, L. [2019] "Power flow and structural intensity analyses of acoustic black hole beams," *Mechanical Systems and Signal Processing* **131**, 538–553.

Zhang, S. and Cheng, L. [2017] "Wavelet decompositions for high frequency vibrational analyses of plates," *International Journal of Applied Mechanics* **9**(6), 1750088.

Zhao, L., Conlon, S. C. and Semperlotti, F. [2014] "Broadband energy harvesting using acoustic black hole structural tailoring," *Smart Materials and Structures* **23**, 065021.

Zhao, L., Conlon, S. C. and Semperlotti, F. [2015a] "Experimental verification of energy harvesting performance in plate-like structures with embedded acoustic black holes," *INTER-NOISE and NOISE-CON Congress and Conference Proceedings*, *Institute of Noise Control Engineering*.

Zhao, L., Conlon, S. C. and Semperlotti, F. [2015b] "An experimental study of vibration based energy harvesting in dynamically tailored structures with embedded acoustic black holes," *Smart Materials and Structures* **24**, 065039.

Zhao, C. and Prasad, M. G. [2018] "Studies on vibration energy harvesting using a cantilever beam with a modified acoustic black hole cavity," *INTER-NOISE Conference Proceedings*, *Institute of Noise Control Engineering*.

Zhao, C. and Prasad, M. G. [2019] "Acoustic black holes in structural design for vibration and noise control," *Acoustics* **1**, 220–251.

Zhou, T. and Cheng, L. [2018] "A resonant beam damper tailored with acoustic black hole features for broadband vibration reduction," *Journal of Sound and Vibration* **430**, 174–184.

Zhou, T., Tang, L., Ji, H., Qiu, J. and Cheng, L. [2017] "Dynamic and static properties of double-layered compound acoustic black hole structures," *International Journal of Applied Mechanics* **9**(5), 1750074.